Acta Cryst. (1999). A**55**, 704–718

Room-temperature and low-temperature structure of $Nd_{1-x}Ca_xMnO_3$ ($0.3 \leq x \leq 0.5$)

O. Richard,[a] W. Schuddinck,[a] G. Van Tendeloo,[a]* F. Millange,[b] M. Hervieu,[b] V. Caignaert[b] and B. Raveau[b]

[a]*EMAT, University of Antwerp (RUCA), Groenenborgerlaan 171, B-2020 Antwerpen, Belgium, and* [b]*Laboratoire CRISMAT, UMR 6508 associé au CNRS, ISMRA et Université de Caen, 6 Boulevard du Maréchal Juin, 14050 Caen CEDEX, France. E-mail: gvt@ruca.ua.ac.be*

(*Received 19 August 1998; accepted 4 March 1999*)

Abstract

The structure of the insulating manganites $Nd_{1-x}Ca_xMnO_3$ ($0.3 \leq x \leq 0.5$) has been studied against temperature using electron diffraction and neutron diffraction. At room temperature, the three compounds with x = 0.3, 0.4 and 0.5 exhibit the orthorhombic $GdFeO_3$-type structure ($a \approx 2^{1/2}a_p$, $b \approx 2a_p$, $c \approx 2^{1/2}a_p$). Below the charge-ordering temperature of ~250 K, a doubling of the lattice is observed along the a axis which could be interpreted as an ordering of the d_{z^2} Mn^{3+} orbitals. The low-temperature polymorph has orthorhombic symmetry for x = 0.5 and monoclinic symmetry for x = 0.4 and 0.3. The low-temperature structure of the x = 0.4 sample was refined using neutron diffraction data. The HREM study at room temperature confirms the average $GdFeO_3$-type structure and indicates the existence of defective areas with a lower symmetry.

1. Introduction

Vigorous investigations have been carried out in the lanthanide manganites $Ln_{1-x}A_xMnO_3$ (A = Ca, Sr, Ba, Pb) since the discovery of 'colossal' magnetoresistance (CMR) in one of these compounds (Kusters *et al.*, 1989). It is now well established that the transport and magnetic properties of these materials are governed by two factors, the hole carrier density (Mn^{3+}/Mn^{4+} ratio) and the size of the interpolated cations (Rodriguez-Martinez & Attfield, 1996; Kumar & Rao, 1997; Sun *et al.*, 1997). Taking into consideration these parameters, it is easy to understand that the double exchange model proposed a long time ago (de Gennes, 1960; Goodenough, 1955) will be at the origin of the CMR effect. This mechanism implies that the electronic exchange between Mn^{3+} and Mn^{4+} species depends strongly on the O—Mn—O angles and the Mn—Mn distances which affect the e_g bandwidth. Moreover, isotope oxygen experiments performed on the manganites (Zhao *et al.*, 1996) suggest that electron–phonon interactions are involved in these properties, so that the Jahn–Teller effect of manganese may also contribute to the CMR effect, as proposed by Millis *et al.* (1995).

From the above statements, it appears that a detailed knowledge of the structure of these manganites is absolutely necessary to understand their behaviour, since tiny structural distortions or modifications of their electronic charge distribution may influence dramatically their transport and magnetic properties. In this respect, the neodymium manganites $Nd_{1-x}(Ca,Sr)_xMnO_3$ are of great interest. A transition is indeed observed, from the ferromagnetic metallic (FMM) to the antiferromagnetic insulating (AFMI) state for $Nd_{0.5}Sr_{0.5}MnO_3$ (Caignaert *et al.*, 1996; Laffez *et al.*, 1996; Tokura *et al.*, 1996). The latter is due to charge-ordering (CO) phenomena, *i.e.* to 1:1 ordering of the Mn^{3+} and Mn^{4+} species that takes place at low temperature, involving a doubling of the lattice parameter and, consequently, an increase of resistivity below the transition.

Our recent study of the perovskite $Nd_{0.7}Ca_{0.3-x}Sr_xMnO_3$ (Millange, Maignan *et al.*, 1996) has renewed interest in these compounds. The structural study of the semiconductor $Nd_{0.7}Ca_{0.3}MnO_3$ (Caignaert *et al.*, 1999; Millange, Caignaert *et al.*, 1996), which does not exhibit any CMR properties up to 5 T, shows a transition from orthorhombic at room temperature to monoclinic below 200 K. The [100] electron diffraction (ED) patterns exhibit very weak 0kl extra reflections indicating an unambiguous change of structure. However, as mentioned above, we need more information to understand the mechanism of the structural transition in these materials. We have therefore used convergent-beam electron diffraction (CBED) to determine the space group and real-space imaging to determine the defective structure. This study has been extended up to the x = 0.5 value.

The manganites $Nd_{1-x}Ca_xMnO_3$ ($0.3 \leq x \leq 0.5$) were studied at room temperature (above the charge-ordering transition $T_{CO} \approx 250$ K) as well as at 100 K for electron diffraction and at 2 K and 175 K for neutron diffraction.

2. Experimental

Samples were prepared by solid-state reaction from the component oxides in appropriate ratios. The reagents were intimately mixed in an agate mortar and heated in air at 1170 K for 12 h to achieve decarbonation. This

Table 1. *'Ideal' symmetries of the different zone-axis patterns for the different point groups belonging to the orthorhombic crystal system*

Orthorhombic	[001]	[010]	[100]	[*uv*0]	[*u*0*w*]	[0*vw*]	[*uvw*]
mmm	(2*mm*)	(2*mm*)	(2*mm*)	(2*mm*)	(2*mm*)	(2*mm*)	(2)
	2*mm*	2*mm*	2*mm*	*m*	*m*	*m*	1
2*mm*	(*m*)	(*m*)	(2*mm*)	(*m*)	(*m*)	(*m*)	(1)
	m	*m*	2*mm*	*m*	*m*	1	1
*m*2*m*	(*m*)	(2*mm*)	(*m*)	(*m*)	(*m*)	(*m*)	(1)
	m	2*mm*	*m*	*m*	1	*m*	1
*mm*2	(2*mm*)	(*m*)	(*m*)	(*m*)	(*m*)	(*m*)	(1)
	2*mm*	*m*	*m*	1	*m*	*m*	1
222	(2*mm*)	(2*mm*)	(2*mm*)	(*m*)	(*m*)	(*m*)	(1)
	2	2	2	1	1	1	1

powder was fired at 1470 K for 12 h. Final firing was performed at 1770 K for five days with intermediate grinding to ensure homogeneity. Phase purity was checked by XRD with a Philips diffractometer using Cu $K\alpha$ radiation.

For electron microscopy, the powder was ground in methanol and the small crystallites were dispersed on a holey carbon grid. The electron diffraction study was carried out with a Philips CM20 operating at 200 kV fitted with a double-tilt ($\pm 30^\circ$) cooling holder. Cooling by liquid nitrogen allowed temperatures of around 100 K to be reached. The HREM studies were performed with a JEOL 4000EX and a Topcon 002B operating at 400 kV and 200 kV, respectively.

Powder neutron diffraction data were collected on the high diffractometer D2B (ILL, Grenoble) with a wavelength of 1.5938 Å. An additional scan was collected with a wavelength of 2.399 Å and a secondary collimator in order to enhance the resolution. Data in the range $15 \leq 2\theta \leq 160^\circ$ were refined by the Rietveld method using the program *Fullprof*.†

3. Results and discussion

3.1. *Electron diffraction*

Electron microdiffraction together with convergent-beam electron diffraction enable us to determine the space group of the different compositions at room temperature as well as at 100 K. The electron microdiffraction patterns allow one to determine the crystal system (Morniroli, 1989; Morniroli & Steeds, 1992), the Bravais lattice, the presence or the absence of glide planes (Ayer, 1989; Morniroli & Gantois, 1990; Morniroli & Steeds, 1992) and the partial extinction symbol ('partial' since this symbol does not take into account the screw axes), which is consistent with a few space groups belonging to different point groups. The point group of the crystal is obtained by observing one or a few convergent-beam electron diffraction patterns (Buxton *et al.*, 1976; Tanaka *et al.*, 1983) or/and electron microdiffraction patterns (Morniroli & Steeds, 1992). The determination of the space group by these techniques requires the observation of high-order Laue-zone reflections. The radius of these zones is often too large and therefore the reflections belonging to these zones are not present on the oriented patterns. To avoid this difficulty, the sample is tilted along the zero-order Laue-zone mirrors until the high-order Laue-zone reflections appear on the pattern. Note that in this section of the paper we will use the conventional axes ($c < a < b$) to facilitate the reading of Tables 1 to 4.

Table 2. *Space groups belonging to the orthorhombic crystal system in agreement with the P— partial extinction symbol*

Point group	222	*mm*2 *m*2*m* 2*mm*	*mmm*
Space group	*P*222	*Pmm*2 *Pm*2*m* *P*2*mm*	*Pmmm*
	$P222_1$ $P22_12$ $P22_12_1$ $P2_122$ $P2_122_1$ $P2_12_12$ $P2_12_12_1$		

3.1.1. *Room-temperature orthorhombic structure from x = 0.3 to x = 0.5.* At room temperature, all compounds exhibit an orthorhombic crystal structure (space group *Pnma*). The study performed on the $Nd_{0.6}Ca_{0.4}MnO_3$ compound is presented below.

The crystal system is obtained from the electron microdiffraction patterns having the highest 'net' symmetries (Morniroli, 1989; Morniroli & Steeds, 1992). These symmetries take into account only the position (not the intensity) of the reflections on the patterns. Three whole patterns [zero-order Laue zone (ZOLZ) + high-order Laue zone (HOLZ)] with the 2 mm 'net' symmetry are obtained (Figs. 1*a*, 1*b* and 1*c*). These

† The numbered intensity of each measured point on the profile is available from the IUCr electronic archives (Reference: SP0160). Services for accessing these data are described at the back of the journal.

symmetries are characteristic of the orthorhombic crystal system. To obtain these patterns (Figs. 1*a*, 1*b* and 1*c*), the sample is tilted along the zero-order Laue-zone mirrors until the first-order Laue-zone reflections appear on the pattern. By using the lattice parameters $a = 5.50$, $b = 7.70$ and $c = 5.40$ Å ($c < a < b$), the zone axes of these patterns are indexed as [001], [010] and [100], respectively. The Bravais lattice, the glide planes and the partial extinction symbol are determined by comparing the experimental patterns with theoretical ones. Taking into account, for each of the crystal systems, the different possibilities of Bravais lattice and of glide plane, all the theoretical electron microdiffraction patterns have been drawn (Morniroli & Steeds, 1992). An individual partial extinction symbol is given for each theoretical microdiffraction pattern. By adding one, two or three individual partial extinction symbols corresponding to different zone-axis patterns (depending on the crystal system), the partial extinction symbol is obtained. For an orthorhombic crystal system,

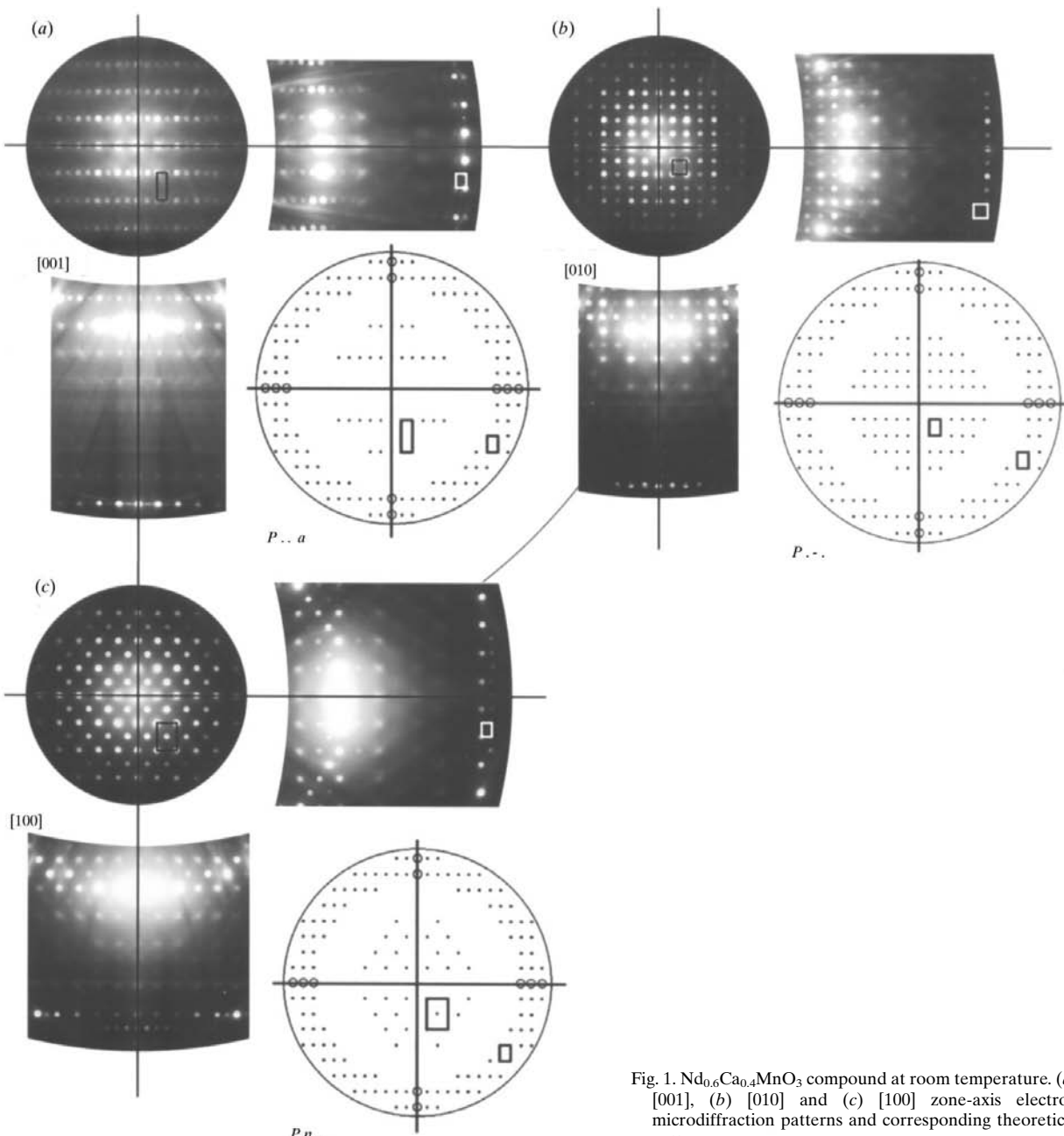

Fig. 1. $Nd_{0.6}Ca_{0.4}MnO_3$ compound at room temperature. (*a*) [001], (*b*) [010] and (*c*) [100] zone-axis electron microdiffraction patterns and corresponding theoretical patterns.

Table 3. *'Ideal' symmetries of the different zone-axis patterns for the different point groups belonging to the monoclinic crystal system*

Monoclinic	[001]	[010]	[100]	[uv0]	[u0w]	[0vw]	[uvw]
2/m	($\underline{2mm}$)	($\underline{2}$)	($\underline{2mm}$)	($\underline{2}$)	($\underline{2mm}$)	($\underline{2}$)	($\underline{2}$)
	$\underline{m}$	$\underline{2}$	$\underline{m}$	$\underline{1}$	$\underline{m}$	$\underline{1}$	$\underline{1}$
m	($\underline{m}$)	($\underline{1}$)	($\underline{m}$)	($\underline{1}$)	($\underline{m}$)	($\underline{1}$)	($\underline{1}$)
	$\underline{m}$	$\underline{1}$	$\underline{m}$	$\underline{1}$	$\underline{m}$	$\underline{1}$	$\underline{1}$
2	($\underline{m}$)	($\underline{2}$)	($\underline{m}$)	($\underline{1}$)	($\underline{m}$)	($\underline{1}$)	($\underline{1}$)
	$\underline{1}$	$\underline{2}$	$\underline{1}$	$\underline{1}$	$\underline{1}$	$\underline{1}$	$\underline{1}$

Table 4. *Space groups belonging to the monoclinic crystal system in agreement with the P1-1 partial extinction symbol*

Point group	2	m	2/m
Space group	$P121$	$P1m1$	$P12/m1$
	$P12_11$		$P12_1/m1$

the determination of the partial extinction symbol requires the analysis of the [001], [010] and [100] zone-axis patterns. On the [001] zone-axis pattern (Fig. 1*a*), the mesh of reflections of the zero-order Laue zone constitutes a noncentred rectangle. The mesh of reflections of the first-order Laue zone (FOLZ) forms a smaller noncentred rectangle. This periodicity difference, between the ZOLZ and the FOLZ, is characteristic of the presence of an *a*-glide plane perpendicular to [001]. Moreover, reflections belonging to the first-order Laue zone are present on the two mirrors. The corresponding theoretical pattern (Fig. 1*a*) has the individual partial extinction symbol *P..a*. A similar analysis is performed for the [010] and [100] zone-axis patterns. The theoretical patterns corresponding to the experimental ones are presented in Figs. 1(*b*) and 1(*c*). The individual partial extinction symbols are *P.-.* and *Pn..*, respectively. The addition of these three individual partial extinction symbols leads to the *Pn-a* partial extinction symbol. This symbol is, according to *International Tables for Crystallography* (1992), in agreement with the $Pn2_1a$ (*m*2*m* point group) and *Pnma* (*mmm* point group) space groups. The point group of the crystal is determined by observing the 'ideal' symmetries of CBED zone-axis patterns. These symmetries take into account the position and the intensity of the reflections. Contrary to the determination of the 'net' symmetries, the determination of the 'ideal' symmetries requires a perfect orientation of the specimen with respect to the electron beam. The zero-order Laue-zone 'ideal' symmetry of the [210] zone-axis pattern (Fig. 2*a*) is ($\underline{2mm}$). To confirm unambiguously that the crystal system is orthorhombic, and not monoclinic, the [301] CBED zone-axis pattern (Fig. 2*b*) is also observed. The 'ideal' symmetry of this pattern is ($\underline{2mm}$). According to Table 1, which gives the zero-order Laue zone and the whole-pattern 'ideal' symmetry for the different zone-axis patterns and for the different point groups belonging to the orthorhombic crystal system (Morniroli & Steeds, 1992), these symmetries are only in agreement with the *mmm* point group. The space group is therefore *Pnma*.

3.1.2. *Low-temperature structure (100 K).*

(*a*) $Nd_{0.7}Ca_{0.3}MnO_3$. On cooling the specimen, very weak extra reflections appear on the electron microdiffraction patterns. The determination of the space group requires that we take into account these extra reflections. Three whole patterns with the 2*mm* 'net' symmetry are presented in Figs. 3(*a*), 3(*b*) and 3(*c*). This indicates that the crystal system is orthorhombic. The patterns can only be indexed by doubling the *a* lattice parameter. Respecting the condition $c < a < b$, the lattice parameters to index these patterns [001], [010] and [100] are then a = 7.70, b = 11.0 and c = 5.40 Å. To obtain the partial extinction symbol, an analysis similar to the one previously described is performed. The individual partial extinction symbols obtained by comparing the experimental [001], [010] and [100] zone-axis patterns with the theoretical ones (Figs. 3*a*, 3*b* and 3*c*) are *P..-*, *P.-.* and *P-..*, respectively. The partial extinction symbol is therefore *P*—. As indicated in Table 2, according to *International Tables for Crystallography* (1992), this symbol is in agreement with 12 space groups belonging to five point groups.

The extra reflections are too weak to allow us to determine the point group from electron microdiffraction patterns and from convergent-beam electron diffraction patterns (Fig. 4). It is worth noting that the crystal system can be monoclinic with a very small distortion. In this case, the partial extinction symbol is

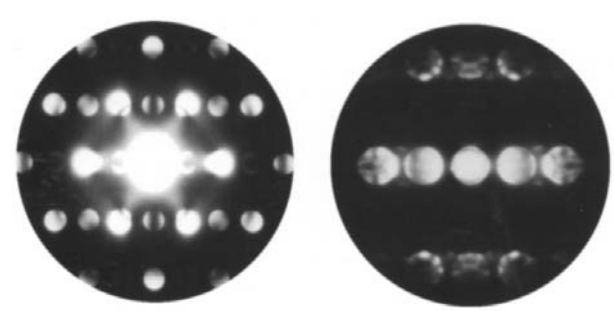

(*a*) (*b*)

Fig. 2. $Nd_{0.6}Ca_{0.4}MnO_3$ compound at room temperature. (*a*) [210] and (*b*) [301] CBED patterns.

*P*1-1. This symbol is according to Table 4 consistent with five space groups belonging to three point groups.

(*b*) *$Nd_{0.6}Ca_{0.4}MnO_3$*. Similar electron microdiffraction patterns to those previously analysed for the $Nd_{0.7}Ca_{0.3}MnO_3$ compound at low temperature (Fig. 3) are obtained. This would seem to indicate that the crystal system is orthorhombic and that the partial extinction symbol is *P*—. The $[110]_{ortho}$ CBED zone-axis pattern (Fig. 5) has (2) 'ideal' symmetry which cannot be in agreement with an orthorhombic crystal system (Table 1). In fact, the crystal system is monoclinic, but the distortion is so small that the crystal system cannot be determined only from the electron microdiffraction patterns. In this case, the partial extinction symbol is *P*- and five space groups, as shown in the Table 4, are consistent with this symbol.

According to Table 4, the (2) 'ideal' symmetry obtained previously (Fig. 5) is consistent with the 2/*m* point group. The space group is therefore *P*2/*m* or $P2_1/m$.

Moreover, Gjønnes & Moodie lines (Gjønnes & Moodie, 1965) are observed in the *h*00 reflections with *h* odd of the [012] electron microdiffraction zone-axis pattern (Fig. 6*a*). These lines appear in kinematically

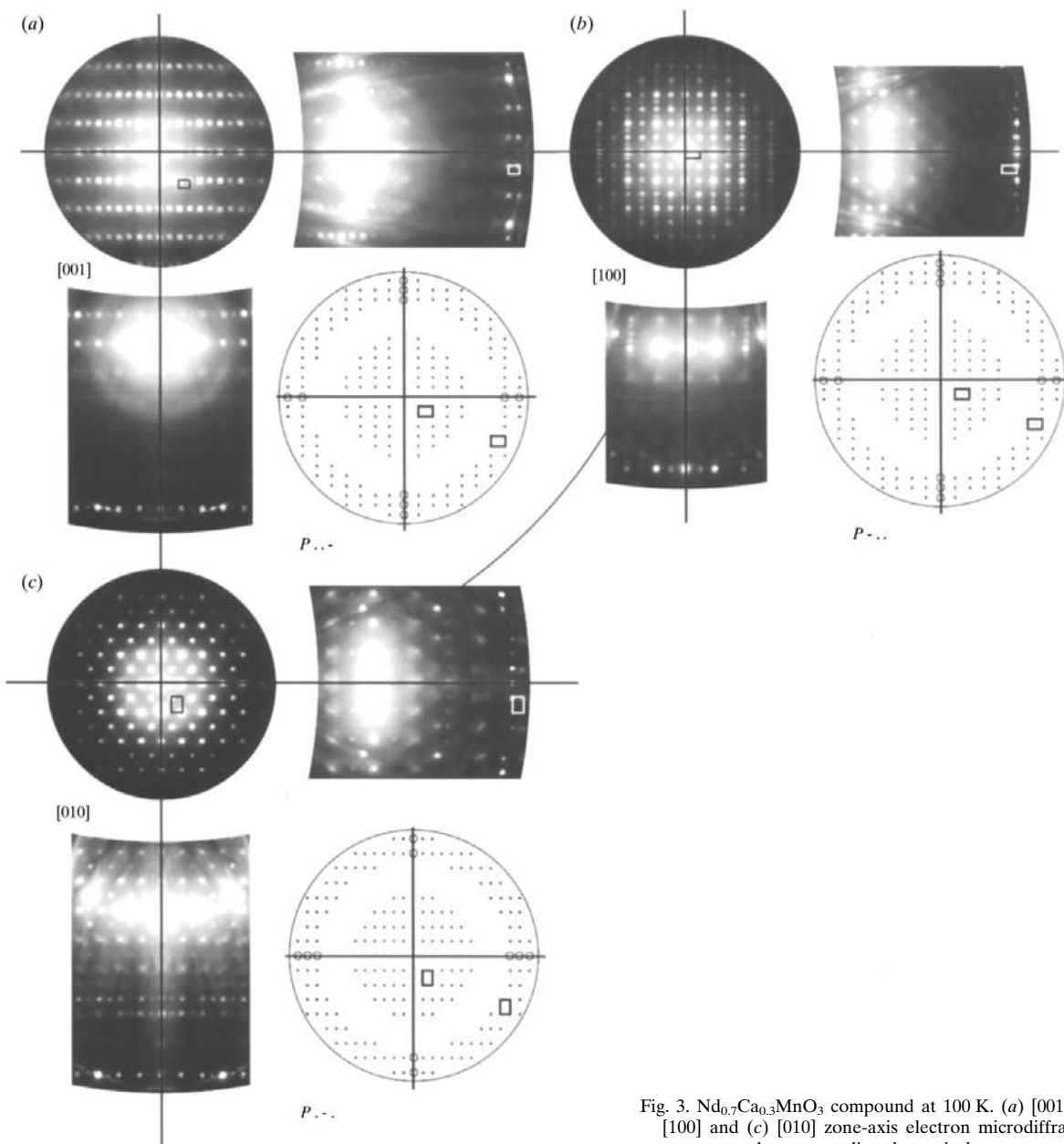

Fig. 3. $Nd_{0.7}Ca_{0.3}MnO_3$ compound at 100 K. (*a*) [001], (*b*) [100] and (*c*) [010] zone-axis electron microdiffraction patterns and corresponding theoretical patterns.

forbidden reflections and are characteristic of a screw axis or a glide plane. By tilting the specimen around the $[100]^*$ axis of the reciprocal lattice, the kinematically forbidden reflections ($h00$ with h odd) disappear (Fig. 6*b*). This proves the presence of a 2_1 screw axis parallel to the *a* axis. The space group is therefore $P2_1/m$.

(*c*) *$Nd_{0.5}Ca_{0.5}MnO_3$*. From the electron microdiffraction patterns, which are similar to those obtained for the $Nd_{0.7}Ca_{0.3}MnO_3$ (Fig. 3) and $Nd_{0.6}Ca_{0.4}MnO_3$ compounds, the $P-$ partial extinction symbol is inferred. 12 space groups belonging to five point groups (Table 2) are in agreement with this symbol. The 'ideal' symmetries of the [110] CBED zone-axis pattern (Fig. 7*a*) are ($\underline{m}$), $\underline{m}$. This is according to Table 1 consistent with the $2mm$ and $m2m$ point groups. The 'ideal' symmetries of the [010] electron microdiffraction zone-axis pattern (Fig. 7*b*) are ($\underline{2mm}$), $\underline{2mm}$. This is in agreement with the mmm and $m2m$ point groups. The point group is therefore $m2m$ and the space group of the $Nd_{0.5}Ca_{0.5}MnO_3$ compound at 100 K is $Pm2m$.

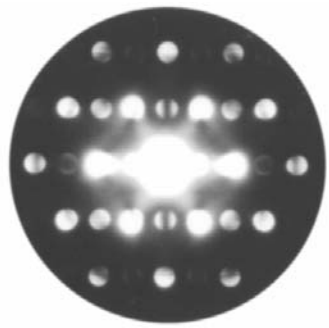

Fig. 4. $Nd_{0.7}Ca_{0.3}MnO_3$ compound at 100 K. $[110]_{ortho}$ CBED pattern.

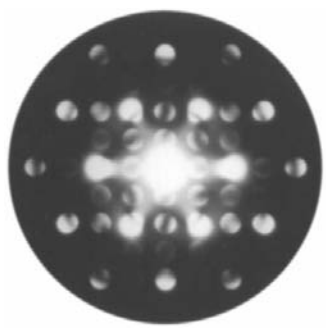

Fig. 5. $Nd_{0.6}Ca_{0.4}MnO_3$ compound at 100 K. $[110]_{ortho}$ CBED pattern.

3.2. *Neutron diffraction*

In this section, as well as in the following one (HREM), the cell parameters of the room-temperature forms refer to the $GdFeO_3$ structure, namely $a \approx 2^{1/2}a_p$, $b \approx 2a_p$, $c \approx 2^{1/2}a_p$ with *Pnma* space group. The low-temperature forms are described by simply considering the doubling of the *a* axis and the *b* axis as unique axis for the monoclinic cells, $a \approx 2^{3/2}a_p$, $b \approx 2a_p$, $c \approx 2^{1/2}a_p$.

3.2.1. *Room-temperature structure*. At room temperature, all three compounds exhibit the orthorhombic $GdFeO_3$ structure ($a \approx 2^{1/2}a_p$, $b \approx 2a_p$, $c \approx$

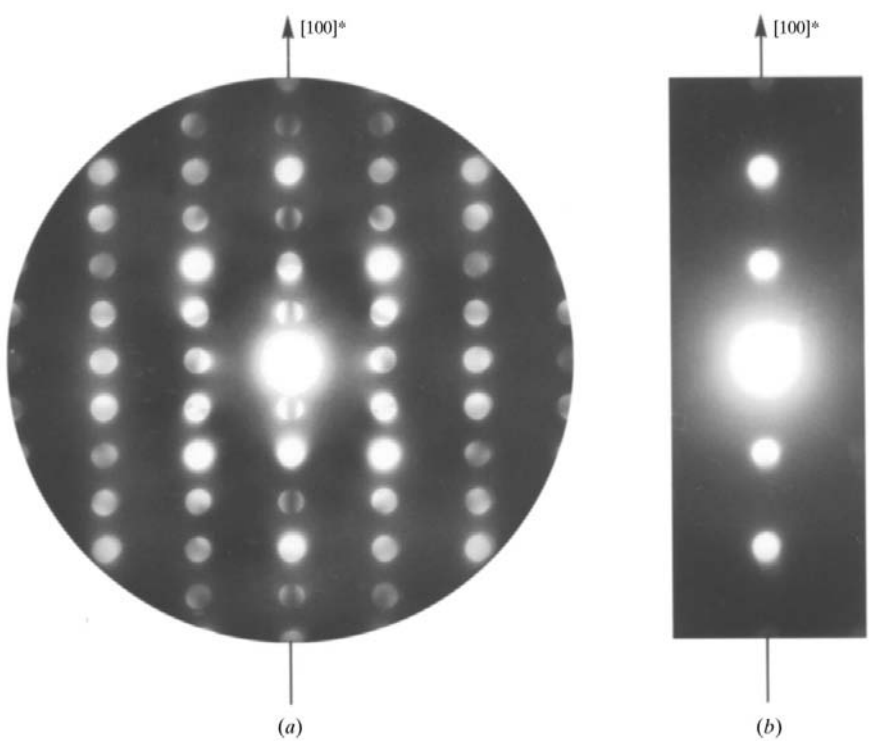

Fig. 6. 2_1 screw axis determination. (*a*) Kinematically forbidden reflections appear by multiple diffraction. (*b*) Kinematically forbidden reflections $h00$ with h odd disappear.

$2^{1/2}a_p$). Refinements of the room-temperature neutron diffraction patterns, carried out in *Pnma* space group, attest to the validity of the structure resolution. Observed, calculated and difference diffraction profiles are shown in Fig. 8. A Jahn–Teller (J–T) distortion of the Q_2 type (antiferrodistortive), which displaces the basal-plane oxygen atoms from their ideal positions, was proposed to be responsible for the insulating state. This distortion does not change the structure symmetry (*Pnma*) but modifies the cell deformation in such a way that $b/2^{1/2} \leq c \leq a$. The resulting Mn—O bond lengths, for $Nd_{0.7}Ca_{0.3}MnO_3$, of 1.992 and 1.953 Å (basal plane) and 1.957 Å (apical distance) are at the origin of a small gap between the J–T split Mn e_g bands ($d_{x^2-y^2}$ and d_{z^2}). The J–T splitting of the e_g band is progressively reduced as the calcium concentration increases in the intermediate $Nd_{1-x}Ca_xMnO_3$ compounds. As a consequence, the distortions are reduced with increasing x in $Nd_{1-x}Ca_xMnO_3$ because the driving force for the J–T distortion is reduced. The corresponding interatomic distances and bond angles are given in Fig. 9. Note that the J–T distortion of the MnO_6 octahedra decreases significantly as x increases, ranging from 1.992 to 1.953 Å for $x = 0.3$, to 1.969–1.946 Å for $x = 0.4$, and to 1.948–1.936 Å for $x = 0.5$. By considering the mean distortion in the MnO_6 octahedra Δd $\{\Delta d = (1/N)\sum_{l=1}^{N}[(d_l - \langle d\rangle/\langle d\rangle]^2\}$, where d corresponds to the Mn—O distances, Table 5 shows that its value is decreased by a factor of 12 as x increases from $x = 0.3$ to $x = 0.5$.

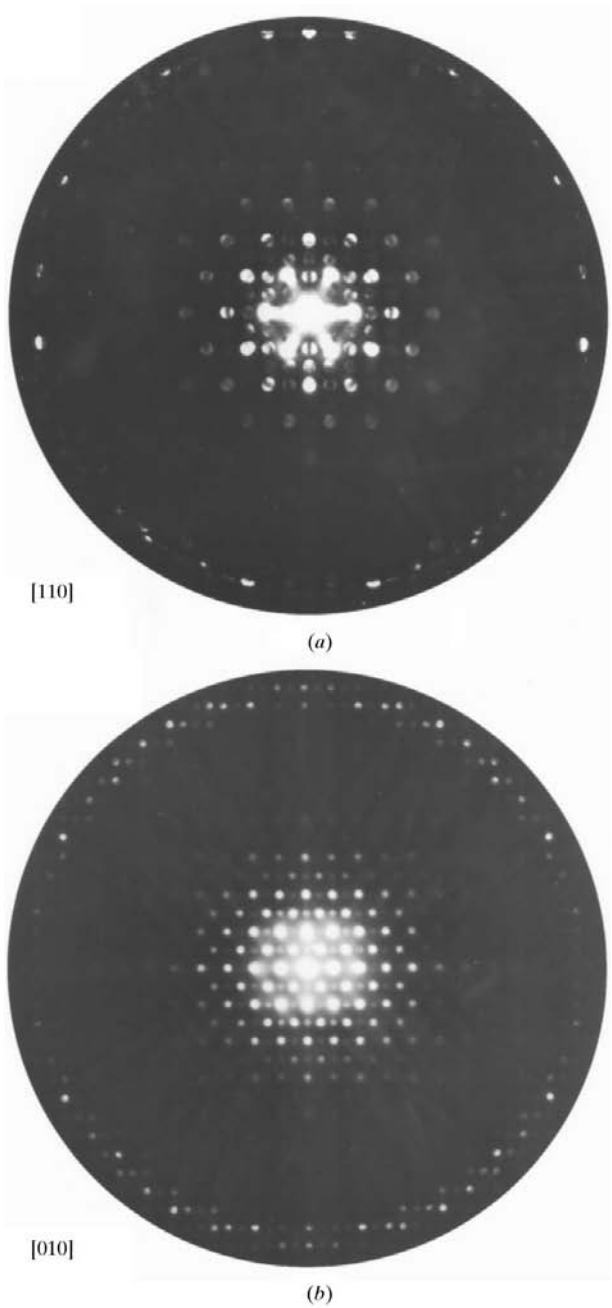

Fig. 7. $Nd_{0.5}Ca_{0.5}MnO_3$ compound at 100 K. (*a*) [110] CBED pattern. (*b*) [010] electron microdiffraction pattern.

3.2.2. *Low-temperature structure*.

(*a*) *$Nd_{0.7}Ca_{0.3}MnO_3$*. The extra reflections observed on the electron diffraction patterns by cooling the specimen are very weak so that the neutron powder diffraction data collected on D2B (ILL) do not allow the pattern to be refined below T_{CO} with a doubling of the lattice along the *a* axis. However, some high-angle peaks in the pattern were split in comparison to the room-temperature phase, indicating that a phase transition occurs with a corresponding lowering of the symmetry from orthorhombic to monoclinic. Refinement was only successful in $P2_1/m$ space group with $a = 5.488$ Å $\approx 2^{1/2}a_p$, $b = 7.634$ Å $\approx 2a_p$, $c = 5.397$ Å $\approx 2^{1/2}a_p$ and $\beta = 90.20°$ at 2 K. Caignaert *et al.* (1999) detected a new type of charge ordering in this compound below T_{CO}. One observes the existence of two different sites for manganese. The Mn(1) sites exhibit an average Mn—O distance of 1.95 Å and can be considered as randomly occupied by both Mn^{4+} (60%) and Mn^{3+} ions (40%). The Mn(2) sites, however, have an average Mn—O distance of 1.968 Å and are supposed to be occupied uniquely by Mn^{3+} ions since the sum of the ionic radii of Mn^{3+} and O^{2-} in sixfold coordination is approximately 1.98 Å. This evidence for ordering of the Mn^{3+} and Mn^{4+} ions is strongly supported by the difference in the Jahn–Teller distortion of the MnO_6 octahedra. With Mn—O distances ranging from 1.953 to 2.033 Å, the Mn(2) octahedra that are uniquely occupied by Mn^{3+} are significantly more distorted than the Mn(1) octahedra (1.913 to 1.981 Å), which are randomly occupied by Mn^{3+} and Mn^{4+} ions.

(*b*) *$Nd_{0.6}Ca_{0.4}MnO_3$*. The existence of charge ordering at low temperature is one of the main issues to be investigated by neutron diffraction. Below T_{CO}, a few extra reflections were observed that could not be

indexed on the basis of the original unit cell with $a \approx 2^{1/2}a_p$, $b \approx 2a_p$, $c \approx 2^{1/2}a_p$, with *Pnma* (Fig. 10*a*). In this space group, the most significant difference between the room-temperature and low-temperature structures occurs in the Mn—O bond lengths. At low temperature, two of the four Mn—O2 distances in the *ac* plane

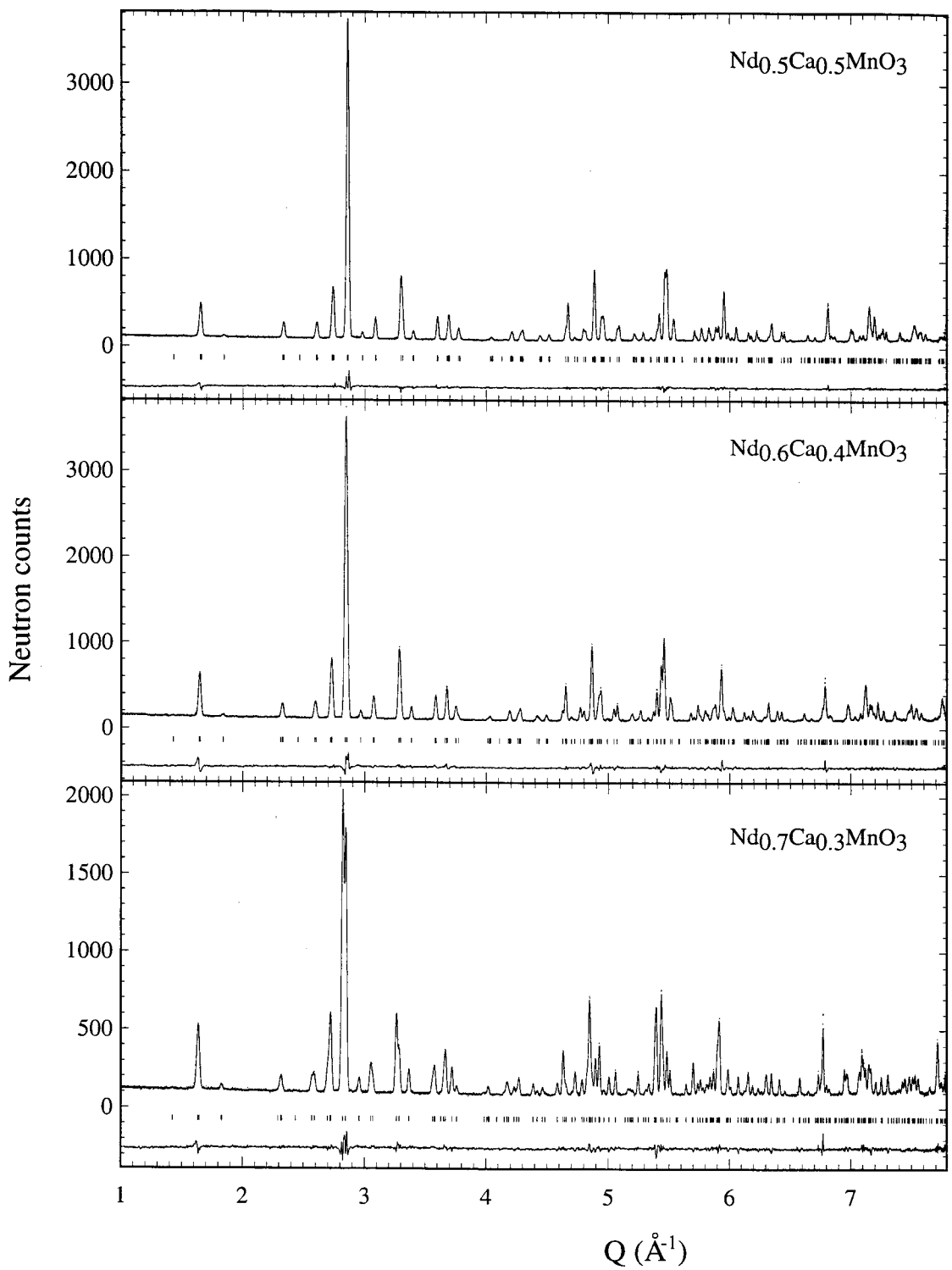

Fig. 8. Observed, calculated and difference diffraction profiles of the x = 0.3, 0.4 and 0.5 samples, recorded at room temperature.

become shorter than the two others (1.972 and 1.943 Å). This result demonstrates the presence of J–T-distorted $Mn^{3+}O_6$ octahedra with the d_{z^2} orbital oriented in the *ac* plane. In agreement with electron diffraction, neutron diffraction refinement was tested in the $P2_1/m$ space group with $a = 10.871$ Å $\approx 2^{3/2}a_p$, $b = 7.574$ Å $\approx 2a_p$, $c = 5.400$ Å $\approx 2^{1/2}a_p$ and $\beta = 90°$ at 175 K. Observed, calculated and difference diffraction profiles are shown in Fig. 10(*b*). This space group can be derived from the aforementioned charge-ordered subgroup of *Pnma* ($P2_1/m$ without cell doubling) by removing one half of the screw axes and the corresponding centres of symmetry located on the Mn(3) atoms. In the $P2_1/m$ structure, the four nonequivalent atoms in the *Pnma* cell are distributed among 15 sets of sites, involving a total of 31 positional parameters (Tables 6 and 7). Although the data are clearly inadequate for a full refinement of this structure, Radaelli *et al.* (1997) have proposed a constrained model based on the average structure with *Pnma* symmetry and the latter is characterized as follows: (i) the O(5), O(6), O(7) and O(8) atoms in the *ac* plane surrounding the Mn(3) atoms were shifted to give a regular undistorted octahedron $Mn(3)O_6$; (ii) the $Mn(3)O_6$ octahedron centred at 1/4, 0, 1/2 was shifted along **c** by Δz while the $Mn(3)O_6$ octahedron centred at 3/4, 0, 1/2 was shifted in the opposite direction; (iii) the Nd/Ca(3) and Nd/Ca(4) atoms were shifted by $\Delta z'$ in the same direction as the neighbouring $Mn(3)O_6$ octahedra (Fig. 11). This model seems to be very satisfactory in view of its simplicity. Based on the value of $\Delta z = 0.01043$, Mn(1) and Mn(2) have two long distances in the *ac* plane, entirely consistent with a J–T distortion of the $Mn(1)O_6$ or/and $Mn(2)O_6$ octahedra.

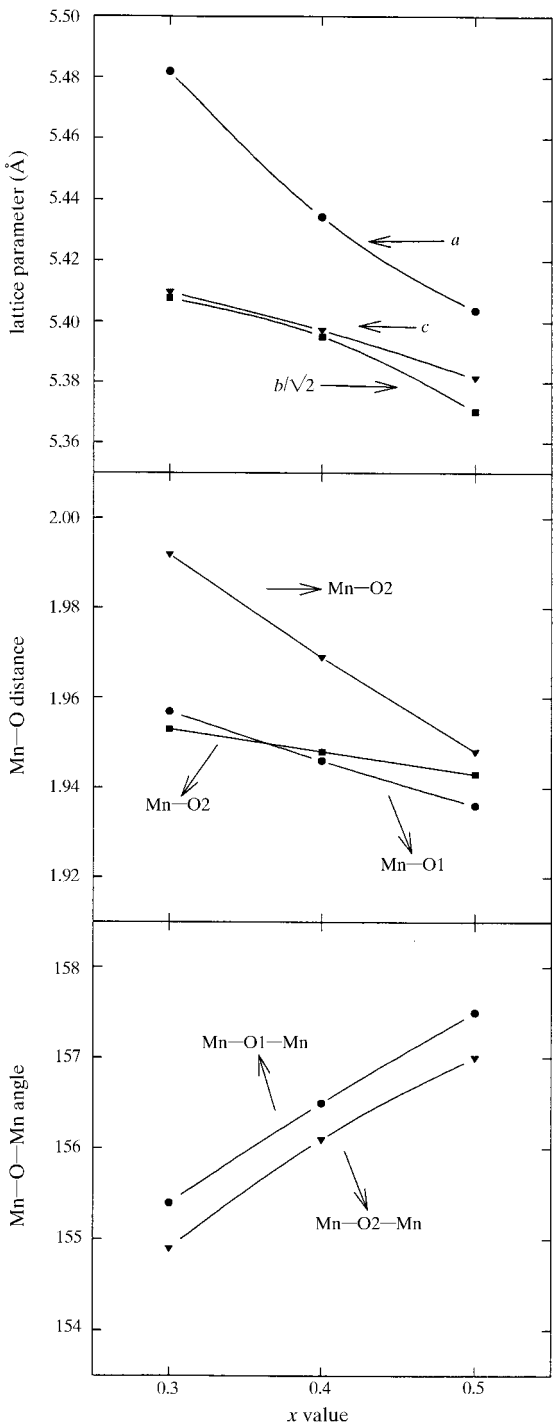

Fig. 9. Calculated interatomic distances and bond angles for $Nd_{1-x}Ca_xMnO_3$ as a function of *x*.

3.2.3. *Room-temperature HREM*. The real-space structure of the three samples ($x = 0.3$, 0.4 and 0.5) was studied using HREM. The [100] and [001] directions on one hand and the [010] and [101] directions on the other hand were selected for imaging. They correspond to the $[110]_p$ and $[100]_p$ directions of the perovskite-type subcell, respectively. This study confirms that, at room temperature, the average structure type is indeed $GdFeO_3$-type, *i.e. Pnma*, but that local anomalies cannot be explained within an orthorhombic structure.

(*a*) *The Pnma structure*. Room-temperature HREM images show very similar contrasts for the three samples. This is in agreement with the theoretical images that have been calculated for the three compounds, on the basis of the positional parameters refined from neutron diffraction (ND) data (Table 5). The good fit between the experimental and calculated [100] and [001] images, which was previously reported for the $x = 0.3$ sample (Caignaert *et al.*, 1999), is also confirmed for the two other compounds ($x = 0.4$ and $x = 0.5$). Fig. 12 is a [010] HREM image recorded for the $x = 0.4$ compound. Its contrast consists of a square-like array of bright dots, spaced 2.7 Å along **a** and **c**, which is that usually observed for perovskite-related compounds.

Domains related by a 90° rotation are currently formed in the 'distorted' perovskite manganites. They are observed not only in the *Pnma* type but also in the *Imma*, *Fmmm* and other perovskite-type structures (Hervieu *et al.*, 1995; Murakami *et al.*, 1997; Chen *et al.*,

1997). They originate from the lowering in symmetry, the superstructure being established along equivalent directions of the perovskite subcell. In that way, the coexistence of [100] and [001] or [101] and [010] oriented domains are commonly observed in the electron diffraction patterns and HREM images. The formation of such domains, which are separated by incoherent boundaries, was previously observed for the $x = 0.3$ sample (Caignaert *et al.*, 1999). Comparison of the three samples shows that they are less visible as x increases. This is related to the amplitude of the distortion which decreases as x increases (Fig. 9).

(*b*) *Deviations from the Pnma structure*. Contrast anomalies, *i.e.* deviations from the expected HREM contrast for the *Pnma*-type structure (experimental *versus* calculated), appear in all three samples. They consist in intensity variations (the so-called 'point-like' defects) which are observed at the level of the Mn atoms surrounded by O atoms. Contrast anomalies have been previously reported for the Pr-based materials (Hervieu

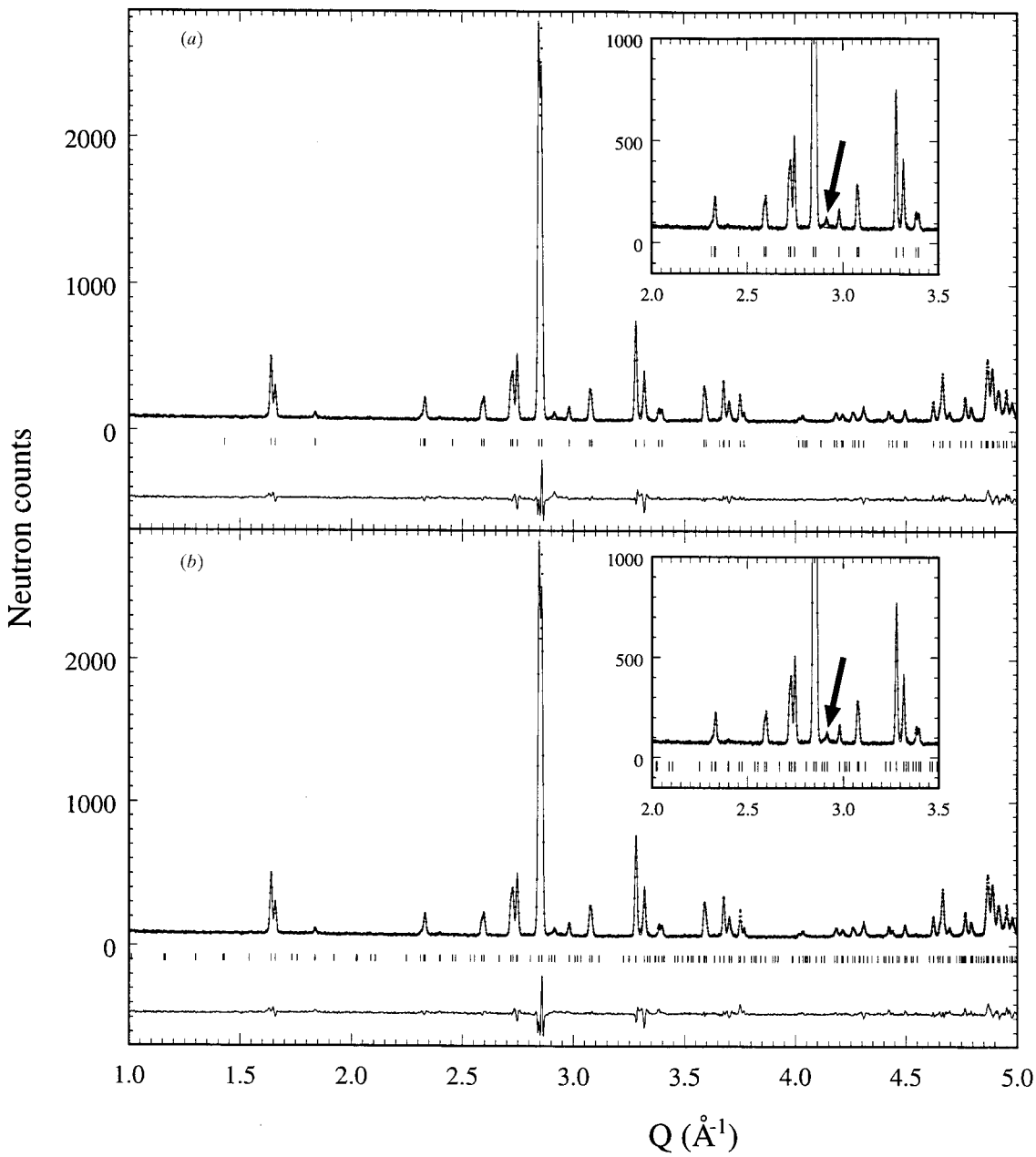

Fig. 10. Low-temperature neutron diffraction pattern of the $x = 0.4$ sample: observed, calculated and difference diffraction profiles by taking into account (*a*) the original unit cell, space group *Pnma* and (*b*) the $a \approx 2^{3/2}a_p$, $b \approx 2a_p$, $c \approx 2^{1/2}a_p$, $\beta = 90°$ unit cell, space group $P2_1/m$.

Table 5. *Room-temperature structures*

Space group: *Pnma*

$Nd_{0.5}Ca_{0.5}MnO_3$			
a = 5.4037 (1) Å			
b = 7.5949 (1) Å			
c = 5.3814 (1) Å			
	x	y	z
Nd/Ca	0.0322 (2)	0.25	−0.0054 (4)
Mn	0	0	0.5
O1	0.4876 (4)	0.0690 (3)	0.25
O2	0.2860 (3)	0.0361 (2)	−0.2856 (2)
Mn−O	11.936 (1) Å	× 2	
Mn−O	21.948 (1) Å	× 2	
Mn−O	21.943 (1) Å	× 2	
Mn−O1−Mn	157.5°		
Mn−O2−Mn	157.0°		
$\Delta_d(10^4)$ 0.064			
R_p = 3.77%			
R_{wp} = 4.84%			
χ^2 = 1.71			

$Nd_{0.6}Ca_{0.4}MnO_3$			
a = 5.4343 (1) Å			
b = 7.6296 (1) Å			
c = 5.3970 (1) Å			
	x	y	z
Nd/Ca	0.0349 (2)	0.25	−0.0057 (4)
Mn	0	0	0.5
O1	0.4862 (3)	0.25	0.0722 (4)
O2	0.2886 (2)	0.0375 (2)	−0.2859 (2)
Mn−O	11.946 (1) Å	× 2	
Mn−O	21.969 (1) Å	× 2	
Mn−O	21.948 (1) Å	× 2	
Mn−O1−Mn	156.5°		
Mn−O2−Mn	156.1°		
$\Delta_d(10^4)$ 0.28			
R_p = 4.14%			
R_{wp} = 5.37%			
χ^2 = 2.03			

$Nd_{0.7}Ca_{0.3}MnO_3$			
a = 5.4820 (1) Å			
b = 7.6475 (1) Å			
c = 5.4096 (1) Å			
	x	y	z
Nd/Ca	0.0400 (2)	0.25	−0.0077 (4)
Mn	0	0	0.5
O1	0.4837 (2)	0.25	0.0752 (3)
O2	0.2917 (2)	0.0393 (1)	−0.2875 (2)
Mn−O	11.957 (1) Å	× 2	
Mn−O	21.992 (1) Å	× 2	
Mn−O	21.953 (1) Å	× 2	
Mn−O1−Mn	155.4°		
Mn−O2−Mn	154.9°		
$\Delta_d(10^4)$ 0.79			
R_p = 4.05%			
R_{wp} = 5.13%			
χ^2 = 1.92			

et al., 1996) and the problem of their origin was tackled. It appears important to find out whether these features are specific for the Pr manganites or if they are observed in other related materials and appear as a more general phenomenon.

Owing to the similarities between the images, for each of the three Nd-based and Pr samples, only two micrographs have been selected and presented to illustrate the mechanism.

The 'point-like' defects appear in the form of abnormally bright or abnormally dark dots, depending on the focus value. One example, recorded for the x = 0.3 sample, is given in Fig. 13(*a*) (for a focus value assumed to be close to −700 Å). The formation of spots that are darker than those of the matrix (some of them are indicated by black triangles) is clearly observed in this [010] image. The density of these point-like defects does not vary with the intensity of the electron beam or with

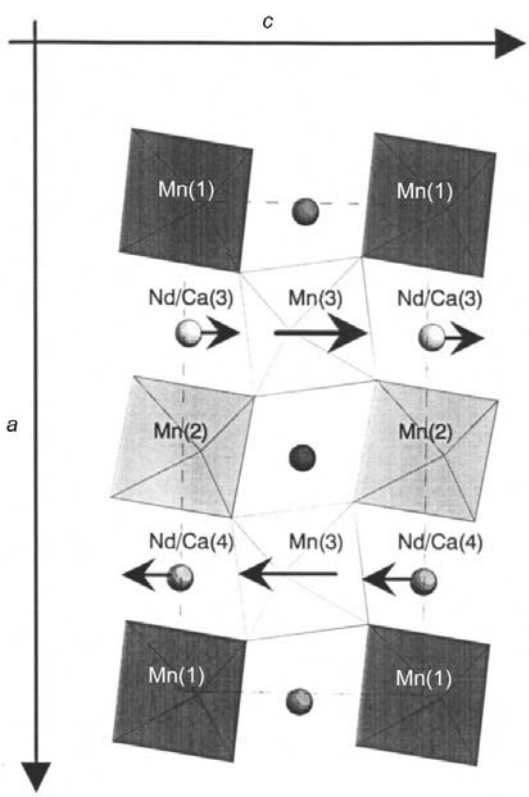

Fig. 11. Projection along **c** of the low-temperature structure (double cell, space group $P2_1/m$).

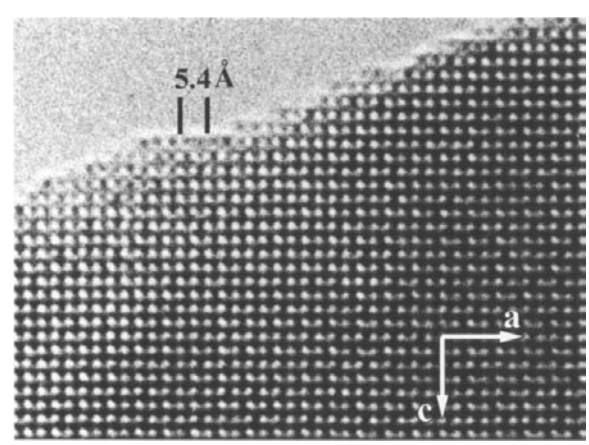

Fig. 12. [010] HREM image of $Nd_{0.6}Ca_{0.4}MnO_3$ illustrating the regular contrast of the *Pnma*-type structure.

the observation time, indicating that they are not radiation induced. The influence of the oxygen atmosphere on the formation of these defects was tested, albeit the neutron diffraction refinements show that the oxygen content of the as-synthesized oxides is close to 3 per perovskite unit. The $x = 0.3$ sample was annealed at 1270 K under O_2 flow and re-observed by HREM. The phenomenon remains and no significant variation of the defect density is observed between the as-synthesized and annealed $x = 0.3$ sample, reinforcing the assumption that oxygen deficiency is not involved in the phenomenon. One observes an effect of clustering along [101] and [10$\bar{1}$] running over a few octahedra (see white arrow). These defects are observed whatever x, from 0.3 to 0.5, with a slightly higher density for $x = 0.5$, which corresponds to the higher Mn^{4+} and Ca contents.

Table 6. *Atomic positions for $Nd_{0.6}Ca_{0.4}MnO_3$ for the 175 K unit-cell structure ($a \approx 2^{1/2}a_p$, $b \approx 2a_p$, $c \approx 2^{1/2}a_p$) with Pnma symmetry*

The numbers after the × sign indicate the site multiplicity.

	x	*y*	*z*	
Mn	0	0	1/2	×4
Nd/Ca	0.0354 (5)	1/4	−0.074 (6)	×4
O(1)	0.4845 (6)	1/4	0.0757 (6)	×4
O(2)	0.2875 (3)	0.0387 (3)	−0.2841 (4)	×8

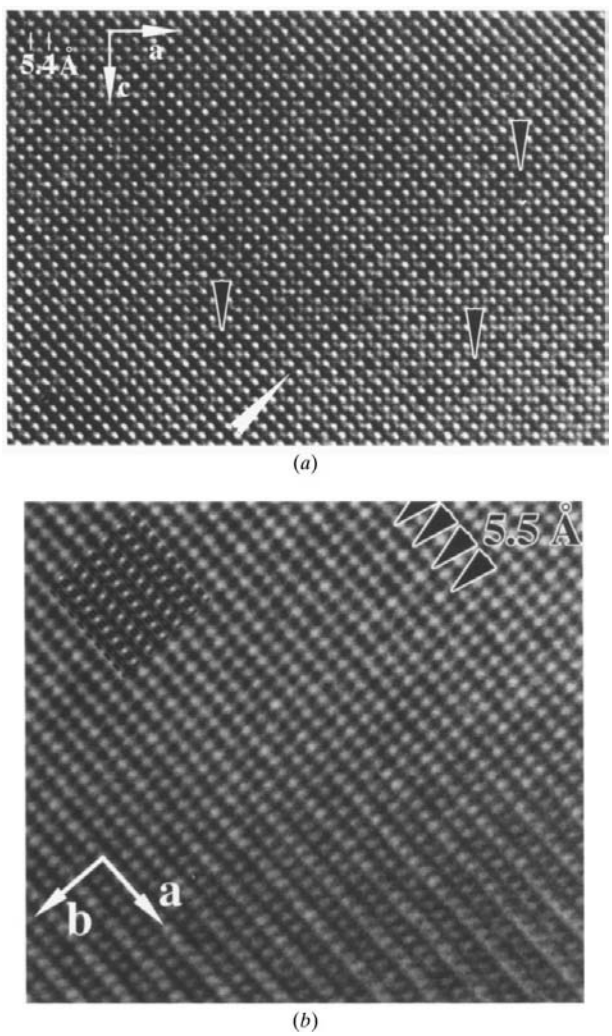

Fig. 13. $Nd_{0.7}Ca_{0.3}MnO_3$ sample: HREM images illustrating the contrast anomalies. (*a*) [010] orientation, the point-like defects appear as darker dots (black arrows). A clustering effect is observed (white arrow). (*b*) [001] orientation, the theoretical image calculated for the *Pnma*-type structure is given in the inset in the left-hand part of the image. The point-like defects appear as brighter dots and the darkening of one row out of two is visible in the bottom part. A local periodicity of 5.5 Å is observed at the level of the $[MnO_2]_\infty$ rows (black arrows).

These 'point-like' defects are also observed by viewing the crystals along [001] (Fig. 13*b*), where the $[MnO_2]_\infty$ layers parallel to (010) appear as rows of bright dots and the $[Nd_{0.7}Ca_{0.3}O]_\infty$ layers appear as the darker rows. The corresponding calculated image for a crystal thickness of 70 Å is shown in the inset; it exhibits a uniform contrast on each type of layer. In this image, it is clearly observed that some of the dots at the level of the $[MnO_2]_\infty$ rows exhibit a brighter contrast. In some areas, a local periodicity of 5.5 Å is observed along **a** (indicated by black triangles). Moreover, another feature is concomitantly observed, which consists in the progressive evolution of the contrast, where the brightness of the dots slowly decreases in one row out of two (bottom part of the image). The periodicity of the intensity variation along **b** is 7.8 Å but the disparity between the 'brightness' of the two $[MnO_2]_\infty$ layers is, here, again not compatible with the [001] (nor with any other equivalent direction of the perovskite subcell) orientation for the refined positional parameters of the *Pnma* orthorhombic structure. The same kind of contrast, consisting of a row of bright dots alternating

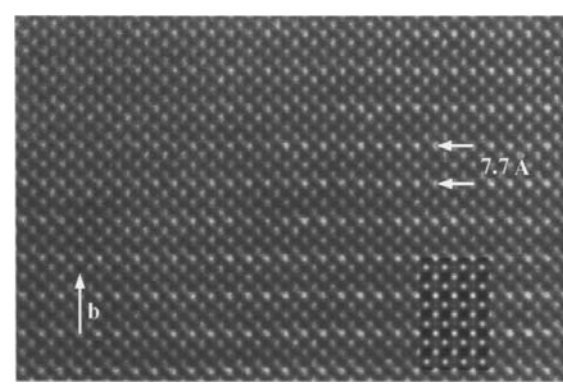

Fig. 14. $Nd_{0.6}Ca_{0.4}MnO_3$ sample: [101] HREM image exhibiting a contrast anomaly consisting of a row of bright dots alternating with a row of grey dots. The calculated image shown as inset is calculated in the $P2_1/c$ space group with a defocus value of −200 Å and a thickness of 50 Å.

with a row of grey dots, is observed by viewing the crystal along [101] (Fig. 14) and is not compatible with the images calculated for the *Pnma* orthorhombic structure.

These results suggest that, at room temperature, local distortions exist, so that the symmetry is only *Pnma* on the average. Such a phenomenon was previously observed for the praseodymium manganites $Pr_{0.7}A_{0.3}MnO_3$, with A = Ca and Sr, whose HREM abnormal contrast was explained by atomic displacements of the oxygen atoms in the $[MnO_2]_\infty$ layers involving a $P2_1/c$ space group, instead of the orthorhombic *Pnma* space group (Hervieu *et al.*, 1996). The present observations show that the neodymium manganites exhibit a similar behaviour.

We have attempted to analyse the contrast anomalies by considering that, locally, the structure may have the monoclinic $P2_1/c$ space group with the following cell parameters: $a_m \approx b_o \approx 2a_p$, $b_m \approx c_o \approx 2^{1/2}a_p$ and $c_m \approx a_o \approx 2^{1/2}a_p$. Thus, using the atomic coordinates of the orthorhombic structure (Table 5), the monoclinic structure (Table 8) is constructed. In the latter, only the O atoms of the $[MnO_2]_\infty$ layers are shifted along the a_m parameter. The $[011]_m$ HREM calculated images for a defocus value of −200 Å and a thickness varying from 30 to 90 Å, *versus* the x_m coordinates are presented in Fig. 15. As expected, since the x_m = 0.54 value is very close to the y_o = 0.5375 value in the orthorhombic structure, the $[011]_m$ calculated images for this x_m exhibit no contrast variation. The contrast anomalies are observed for the other values of x_m. The $[011]_m$ theoretical image obtained for a thickness of 50 Å and x_m = 0.58, shown as the inset in Fig. 14, is in agreement with the experimental image. Image simulations (defocus of

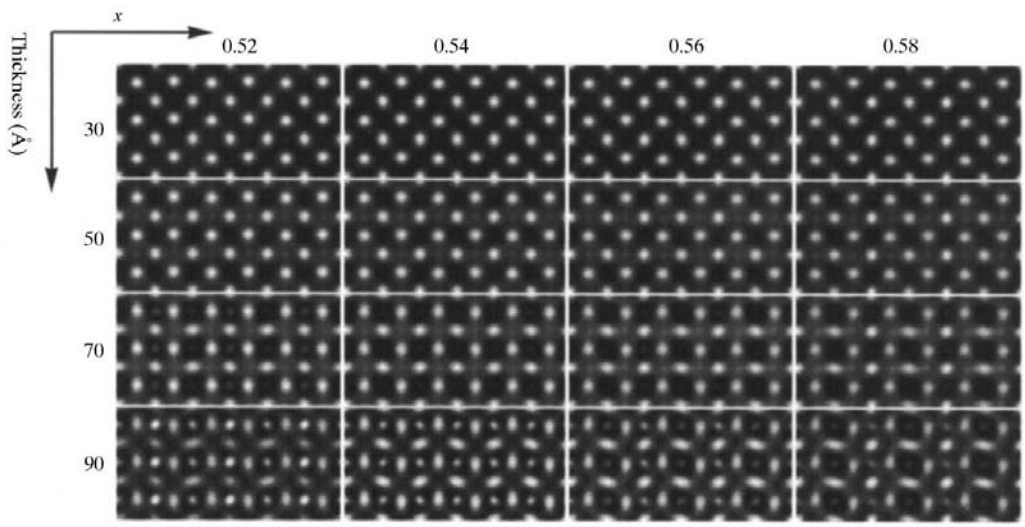

Fig. 15. $[011]_m$ theoretical images calculated for a defocus of −200 Å *versus* thickness and x_m value.

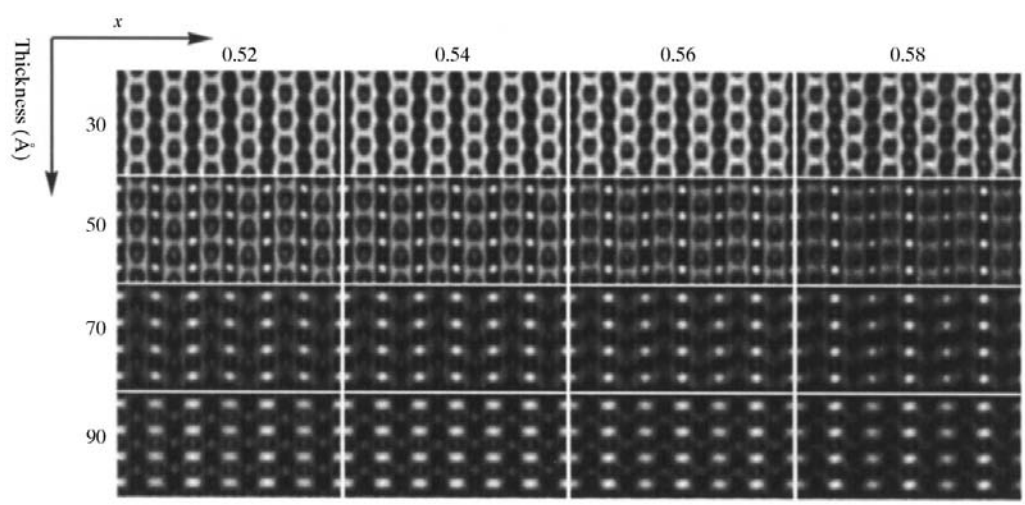

Fig. 16. $[010]_m$ theoretical images calculated for a defocus of −700 Å *versus* thickness and x_m value.

Table 7. *Atomic positions for $Nd_{0.6}Ca_{0.4}MnO_3$ for the 175 K structure, based on the double cell ($a \approx 2^{1/2}a_p$, $b \approx 2a_p$, $c \approx 2^{1/2}a_p$) with $P2_1/m$ symmetry*

The average positional parameters were fixed to the values obtained from a Rietveld fit to the xtructure with the *Pnma* symmetry, based on the same data. The fit yields $\Delta z = 0.01043$ and $\Delta z' = 0.01152$.

	x	y	z	
Mn(1)	0	0	0	×2
Mn(2)	1/2	0	0	×2
Mn(3)	1/4	0	$0.5+\Delta z$	×4
Nd/Ca(1)	0.0177	1/4	0.4925	×2
Nd/Ca(2)	0.5177	1/4	0.4925	×2
Nd/Ca(3)	0.2677	1/4	$0.0074+\Delta z'$	×2
Nd/Ca(4)	0.7677	1/4	$0.0074-\Delta z'$	×2
O(1)	0.2422	1/4	$0.5757+\Delta z$	×2
O(2)	0.7422	1/4	$0.5757-\Delta z$	×2
O(3)	0.4922	1/4	0.9242	×2
O(4)	0.9922	1/4	0.9242	×2
O(5)	0.1437	0.0387	$0.2159+\Delta z$	×4
O(6)	0.6437	0.0387	$0.2159-\Delta z$	×4
O(7)	0.3937	0.0387	$0.2841+\Delta z$	×4
O(8)	0.8937	0.0387	$0.2841-\Delta z$	×4

Table 8. *Atomic positions for $Nd_{0.6}Ca_{0.4}MnO_3$ at room temperature, $a_m = 7.63$, $b_m = 5.40$, $c_m = 5.43$ Å, $\beta = 90^\circ$, monoclinic, space group $P2_1/c$*

x_m: value that has been varied.

	x	y	z	
Nd/Ca	1/4	0.9943	0.0349	×4
Mn(1)	0	1/2	0	×2
Mn(2)	1/2	1/2	0	×2
O(1)	1/4	0.0722	0.4862	×4
O(2)	0.0375	0.7141	0.2886	×4
O(3)	x_m	0.2859	0.7114	×4

−700 Å) performed for the $[001]_o$ ($[010]_m$) zone axis are presented in Fig. 16. As above, the $x_m = 0.54$ images correspond to the orthorhombic structure, *i.e.* no contrast variations are observed. The anomaly contrast is observed for the other values of x_m.

These HREM observations show that the existence of point-like defects and the local lowering of the symmetry from orthorhombic to monoclinic at room temperature are not specific for the manganites $Pr_{0.7}A_{0.3}MnO_3$, but are also observed for $Nd_{1-x}Ca_xMnO_3$ ($0.3 \leq x \leq 0.5$). It is important to note that the local monoclinic distortion observed at room temperature might be the premise to the charge ordering that appears at low temperature. In order to understand the relationship between these phenomena, a comparative study of the samples at low and room temperature and a study of the influence of other factors, such as Mn doping, upon the structure and microstructure of these phases will be carried out.

4. Conclusions

Three $Nd_{1-x}Ca_xMnO_3$ ($0.3 \leq x \leq 0.5$) compounds have been studied at room temperature as well as below the charge-ordering temperature by electron microscopy and neutron diffraction.

From electron microdiffraction, CBED and neutron diffraction, the three compounds (x = 0.3, 0.4 and 0.5) are shown to exhibit the orthorhombic $GdFeO_3$-type structure ($a \approx 2^{1/2}a_p$, $b \approx 2a_p$, $c \approx 2^{1/2}a_p$) with space group *Pnma* at room temperature. High-resolution images confirm this result but local distortions that cannot be explained within an orthorhombic structure are observed. These local anomalies have been simulated by slightly shifting the oxygen atoms which are in the $[MnO_2]_\infty$ layers involving a $P2_1/c$ space group which might be at the origin of the charge ordering that appears at low temperature.

On cooling the three samples below the charge-ordering temperature, extra reflections, characteristic of the doubling of the a lattice parameter, appear in electron diffraction.

In the case of the $Nd_{0.7}Ca_{0.3}MnO_3$ compound, these reflections are very weak and the space group has not been unambiguously inferred from electron microdiffraction and CBED. Neutron diffraction exhibits no extra peaks but a splitting of some high-angle peaks, indicating a phase transition with a lowering of the symmetry from orthorhombic to monoclinic. The neutron diffraction pattern has been refined in space group $P2_1/m$ with $a = 5.488$ Å $\approx 2^{1/2}a_p$, $b = 7.634$ Å $\approx 2a_p$, $c = 5.397$ Å $\approx 2^{1/2}a_p$ and $\beta = 90.20^\circ$ at 2 K.

For the $Nd_{0.6}Ca_{0.4}MnO_3$ compound, the $P2_1/m$ space group is inferred from electron microdiffraction and convergent-beam electron diffraction. The obtained neutron diffraction pattern is compatible with this space group.

Electron microdiffraction and convergent-beam electron diffraction patterns of the $Nd_{0.5}Ca_{0.5}MnO_3$ compound point towards $Pm2m$ space group.

Authors are grateful to Dr E. Suard (Institut Laue–Langevin, Grenoble, France) for neutron diffraction facilities and valuable advice. IUAP 4/10 and FWO-Belgium are acknowledged for financial support.

References

Ayer, R. (1989). *J. Electron Microsc. Tech.* **13**, 16–26.
Buxton, B. F., Eades, J. A., Steeds, J. W. & Rackham, G. M. (1976). *Proc. R. Soc. London Ser. A*, **281**, 171–194.
Caignaert, V., Millange, F., Hervieu, M., Mather, G. & Raveau, B. (1999). *Phys. Rev. B*. In the press.
Caignaert, V., Millange, F., Hervieu, M., Suard E. & Raveau, B. (1996). *Solid State Commun.* **99**, 173–177.
Chen, C. H., Cheong, S. W. & Hwang, H. Y. (1997). *J. Appl. Phys.* **81**, 4326–4330.
Gennes, P. G. de (1960). *Phys. Rev.* **118**, 141–154.
Gjønnes, J. & Moodie, A. F. (1965). *Acta Cryst.* **19**, 65–67.

Goodenough, J. B. (1955). *Phys. Rev.* **100**, 564–573.
Hervieu, M., Masheh, R., Rangavittal, N. & Rao, C. N. R. (1995). *Eur. J. Solid State Inorg. Chem.* **32**, 79–94.
Hervieu, M., Van Tendeloo, G., Caignaert, V., Maignan, A. & Raveau, B. (1996). *Phys. Rev. B*, **53**, 14274–14284.
International Tables for Crystallography (1992). Vol. A, edited by Th. Hahn. Dordrecht: Kluwer Academic Publishers.
Kumar, N. & Rao, C. N. R. (1997). *J. Solid State Chem.* **129**, 363–366.
Kusters, R. M., Singleton, J., Keen, D. A., McGreevy, R. & Hayes W. (1989). *Physica (Utrecht)*, B**155**, 362–365.
Laffez, P., Van Tendeloo, G., Millange, F., Caignaert, V., Hervieu M. & Raveau, B. (1996). *Mater. Res. Bull.* **31**, 905–911.
Millange, F., Caignaert, V., Mather, G., Suard, E. & Raveau, B. (1996). *J. Solid State Chem.* **127**, 131–135.
Millange, F., Maignan, A., Caignaert, V., Simon, C. & Raveau, B. (1996). *Z. Phys. B*, **101**, 169–174.
Millis, A. J., Littlewood, P. B. & Shraiman, B. I. (1995). *Phys. Rev. Lett.* **74**, 5144–5147.
Morniroli, J. P. (1989). *Inst. Phys. Conf. Ser.* **98**, 87–90.
Morniroli, J. P. & Gantois, M. (1990). Proc. 12th International Congress for Electron Microscopy, Vol. 2, pp. 478–479.
Morniroli, J. P. & Steeds, J. W. (1992). *Ultramicroscopy*, **45**, 219–239.
Murakami, Y., Shindo, D., Chiba, H., Kikuchi, M. & Syono, Y. (1997). *Phys. Rev. B*, **55**, 15043–15047.
Radaelli, P. G., Cox, D. E., Marezio, M. & Cheong, S.-W. (1997). *Phys. Rev. B*, **55**, 3015–3023.
Rodriguez-Martinez, L. M. & Attfield, J. P. (1996). *Phys. Rev. B*, **54**, R15622–15625.
Sun, J. R., Rao, G. H. & Liang, J. K. (1997). *Appl. Phys. Lett.* **70**, 1900–1902.
Tanaka, M., Saito, R. & Sekii, H. (1983). *Acta Cryst.* A**39**, 357–368.
Tokura, Y., Huwahara, H., Moritomo, Y., Tomioka, Y. & Asamitsu, A. (1996). *Phys. Rev. Lett.* **76**, 3184–3191.
Zhao, G., Conder, K., Keller H. & Müller, K. A. (1996). *Nature (London)*, **381**, 676–678.